Chapter 1
Hydrogen Migration in Intense Laser Fields: Analysis and Control in Concert

Nicola Reusch, Nora Schirmel and Karl-Michael Weitzel

Abstract The dissociative ionization of ethane leading to the formation of H^+, H_3^+ and CH_3^+ ions has been studied in femtosecond laser fields. The analysis of kinetic energy distributions of the ions provides information on the mechanism of the photodynamics involved. Important ingredients of these dynamics are hydrogen migration, charge localization and charge separation. We demonstrate that it is possible to go one step beyond analysis towards the control of product yields. Ultimately, controlling the yields of branching ratios provides us with even improved understanding of the competing reaction pathways.

1.1 Introduction

In recent years we have seen major progress in the field of photodynamics of molecules and molecular ions induced by intense ultra-short laser fields [1–7]. Not only have we increased our understanding of bond-breaking, but also that of bond-making [8, 9]. A prototypical example in this context is the formation of H_3^+ ions in the dissociative ionization of several small hydrocarbon molecules employing femtosecond laser pulses [10–13]. The equilibrium geometry of the H_3^+ ion is that of an equilateral triangle [14]. Forming this species from a saturated hydrocarbon molecule obviously involves the breaking of three C–H bonds and also the formation of one two-electron-three-center bond. Let us recall the case of fs-laser ionization mass spectrometry (fs-LIMS) of ethane. Here, the dissociative ionization leads to a broad range of ion signals arising in part from single ionization, but in part also from multiple ionization. One of the fragment ions is the H_3^+ ion, whose formation, as we have shown in previous work, proceeds on the doubly charged potential energy surface [13]. The doubly charged ethane ion, $C_2H_6^{++}$, has a well bound equilibrium

N. Reusch · N. Schirmel · K.-M. Weitzel (✉)
Fachbereich Chemie, Philipps-Universität Marburg, 35032 Marburg, Germany
e-mail: weitzel@chemie.uni-marburg.de

geometry which can be viewed as a CH_4^{++} ion attached to a CH_2 moiety [15]. Since the initial ionization is a vertical event, visiting that region of phase space, where the equilibrium geometry is located, requires a hydrogen migration. This at the same time constitutes a certain time requirement for this process to occur. The process also involves the rearrangement of electron density with aspects of charge localization and charge separation. Early hints at the relevance of hydrogen migration in fs-laser ionization came from isotope labeling experiments [16]. E.g. the dissociative ionization of deuterated methanol CH_3OD leads to the observation of both H_3^+ and H_2D^+, where the latter again requires hydrogen/deuterium migration [17, 18]. In order to better understand the photodynamics of ethane, we have employed a variety of different techniques in the past. Our first experimental investigation was focused on the average kinetic energy release (KER) in the dissociative ionization of ethane leading to the formation of H_3^+ and $C_2H_3^+$ [13]. At the relevant laser pulse conditions ($>80\,\mu J$) the kinetic energies of H_3^+ and $C_2H_3^+$ were momentum matched indicating that the two ions were formed in the Coulomb explosion of a common precursor, i.e. the $C_2H_6^{++}$ ion. This interpretation was supported by the first complete reaction path obtained by means of high level ab initio calculations leading from the ethane dication to the fragments $H_3^+ + C_2H_3^+$ [13].

Subsequently, we further confirmed this mechanism by means of an ion-ion-coincidence investigation of the correlated formation of the fragments H_3^+ and $C_2H_3^+$ [19]. In that work we also detected coincidences between other pairs of fragments, e.g. H^+ and $C_2H_5^+$. At first glance it appeared surprising that the $H^+ + C_2H_5^+$ channel exhibited a clear anisotropy, indicating fast decay of the precursor, yet the intensity was much lower than that for the $H_3^+ + C_2H_3^+$ channel, which was isotropic, hence indicating a lifetime of the precursor longer than a rotational period. This puzzle can be resolved by realizing that most of the H^+ signal in fact does not correlate with $C_2H_5^+$ but with $C_2H_3^+ + H_2$ [20]. Thus, the H^+ ions observed in coincidence with $C_2H_5^+$ constitute a minority channel, although formed with a very short time constant. The formation of H_3^+ ions on the other hand, which certainly occurs in coincidence with $C_2H_3^+$ ions, is a majority channel, which involves the migration of hydrogen atoms over several energetically low lying transition states indicated in Fig 1.1 before passing the final rate-limiting transition state leading to product formation.

In this work we complement previous investigations aimed at understanding the molecular dynamics involved in the dissociative ionization of ethane by studies aimed at controlling the yields of the different molecular processes involved. We will first review very recent work employing *linear* chirp as a tool for controlling fragmentation yields [21]. We will further complement that work by employing *quadratic* chirp as well as the concept of genetic algorithms. Experimentally we will not only present ion yields but also kinetic energy distributions (KED) as a function of the laser pulse parameters.
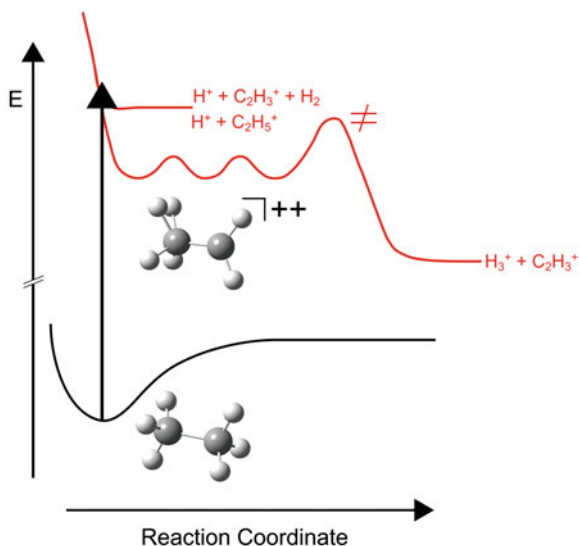
Fig. 1.1 Schematic illustration of the potential energy curves leading from the equilibrium conformation of the neutral ethane (*lower curve*) to the formation of H^+ and H_3^+ on the dicationic state. The characteristics of the potential energy curve for the H_3^+ formation illustrates the corresponding hydrogen scrambling and the transition states involved

1.2 Experimental Approach

All experiments have been carried out employing femtosecond laser pulses delivered by a multipass amplifier (Quantronix, ODIN) operated at a repetition rate of 1 kHz and seeded by a Ti:Sapphire oscillator (SYNERGY, Femtolasers). The wavelength of these pulses is typically centered at about 810 nm. The spectral bandwidth is on the order of 40 nm. The spectral phase was controlled by using a spatial light modulator (SLM-S640, Jenoptik, 640 pixel, nematic liquid crystal mask, 430–1,600 nm) in a folded 4f-shaper setup. The shortest laser pulses accessible with this laser system are typically 45 fs. The laser pulses were characterized using a frequency-resolved optical gating technique (FROG, GRENOUILLE 8-50, Swamp Optics). Experiments running the GRENOUILLE in the spatial mode confirm that a spatial chirp, which could possibly be introduced in the 4f-shaper, is negligible. The laser pulse energies used in the current study are in the range between 10 and 150 μJ, which, when focused by an $f = 75$ mm mirror (leading to a focal radius of 40 μm, as measured by the knife-edge technique), correspond to 4.4×10^{12} and 6.6×10^{13} W/cm^2 in the case of the 45 fs pulses. These laser pulses are focused into the ion source of a home-built time-of-flight mass spectrometer (ToF-MS), which mainly consists of three electrostatic lenses with a distance of 14 mm to each other and a field free drift tube (59.7 cm). The field strength in the ion source was 250 V/cm. All ions are detected by a microchannel plate device, all signals are processed in a personal

computer employing the LabVIEW suit of programs. The sample (ethane, Fluka, 99.95 % purity) is introduced effusively into the experimental chamber.

The pivotal property for characterizing femtosecond laser pulses is the phase. Here, we choose to discuss the spectral phase of the laser field, which can be expanded as a Taylor series:

$$\varphi(\omega) = \varphi_0 + (\omega - \omega_0) \cdot \frac{1}{1!} \cdot \left.\frac{\partial \varphi}{\partial \omega}\right|_{\omega=\omega_0} + (\omega - \omega_0)^2 \cdot \frac{1}{2!} \cdot \left.\frac{\partial^2 \varphi}{\partial \omega^2}\right|_{\omega=\omega_0}$$
$$+ (\omega - \omega_0)^3 \cdot \frac{1}{3!} \cdot \left.\frac{\partial^3 \varphi}{\partial \omega^3}\right|_{\omega=\omega_0} + \cdots \tag{1.1}$$

The third term in (1.1) describes a quadratic spectral phase which causes a linear chirp. The linear chirp parameter α is given by

$$\alpha = \frac{1}{2!} \cdot \left.\frac{\partial^2 \varphi}{\partial \omega^2}\right|_{\omega=\omega_0} \tag{1.2}$$

By writing a quadratic spectral phase on the spatial light modulator (SLM) in the 4f-shaper setup, also shown in Fig. 1.2, a linear chirp is imprinted onto the laser pulse. This is accompanied by a temporal stretching of the pulse according to (1.3), where τ_0 is the pulse duration (full width half maximum, FWHM) of the shortest pulse achieved [22].

$$\tau^2 = \tau_0^2 + \left(\frac{8 \cdot \ln 2 \cdot \alpha}{\tau_0}\right)^2 \tag{1.3}$$

In the same manner a quadratic chirp (third order dispersion, TOD) is generated by writing a third order spectral phase onto the SLM. The quadratic chirp is described by the fourth term in the Taylor series and characterized by the chirp parameter β given by

$$\beta = \frac{1}{3!} \cdot \left.\frac{\partial^3 \varphi}{\partial \omega^3}\right|_{\omega=\omega_0} \tag{1.4}$$

Pure quadratic chirp can be considered to introduce pre-pulses, respectively post-pulses. A good overview of pulse shapes and their description is given in [23]. We will present a visualization of typical laser fields for pulse shapes used in this work in the results section.

While the *linear* and the *quadratic* chirp discussed above may be considered as systematic pulse shaping, we have also performed experiments where we searched for the optimum laser field maximizing certain ion yields. The properties of the laser fields which are varied in order to maximize a specific objective, e.g. the ion yield, are the spectral phase, i.e. the phase in the frequency domain. The experimental
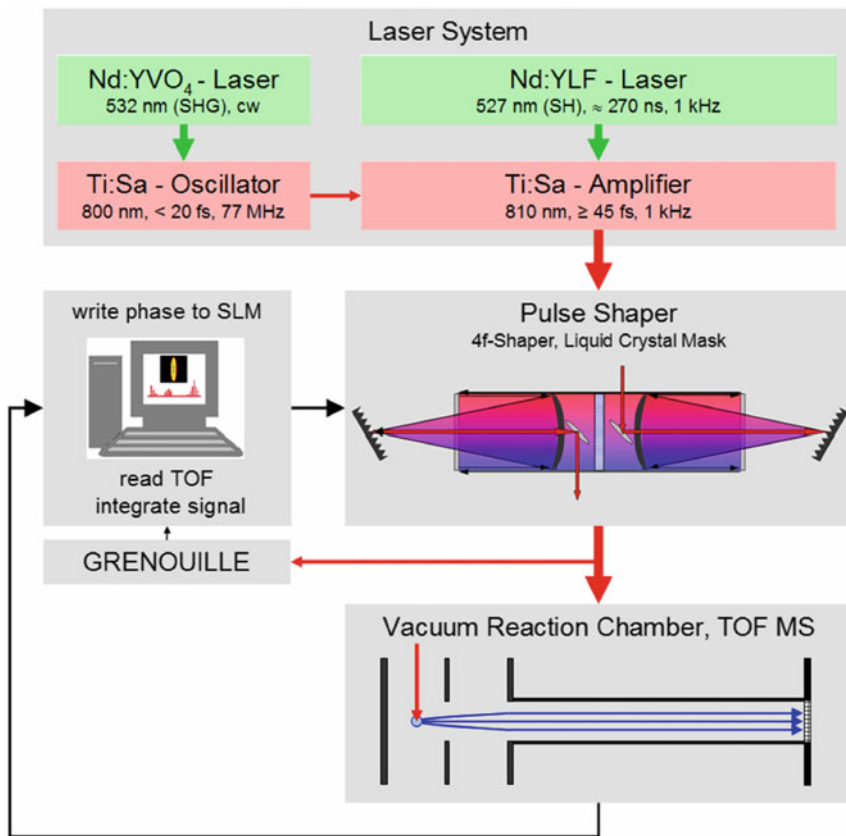
Fig. 1.2 Schematic setup of the experiment including the laser system, the pulse shaper with the spatial light modulator (SLM), the time-of-flight mass spectrometer and the data acquisition system. The main technique for pulse characterization is frequency resolved optical gating (FROG, GRENOUILLE)

device for varying the spectral phase is the SLM which is part of the 4f-shaper setup indicated in Fig. 1.2. We optically expand the laser pulse over as many pixels on the SLM as possible. Each pixel can be assigned an independent phase value between 0 and 2π. This spans an enormous parameter space, which we cannot scan manually. Instead we use a genetic algorithm to solve this optimization problem. The algorithm used by us is one delivered with the SLM but was adapted to our experimental setup [24]. The actual program used consists of two parts, one to control the data acquisition and the second one to execute the genetic algorithm.

In the context of this optimization task a spectral phase is defined by a set of 640 spectral phase parameters (genes, one per pixel). This is termed an individual in evolutionary algorithms. The first part of the program writes this spectral phase to the SLM. For each individual 500 ToF mass spectra are recorded and averaged. A baseline correction is performed and the observable of interest is extracted from

this spectrum, e.g. the integrated H_3^+ ion yield. This integrated ion yield then serves as the fitness value for the genetic algorithm. The next higher level of hierarchy is the generation. Each generation typically consists of 40 individuals, for which the ToF measurement and analysis is repeated. The second part of the program analyzes these 40 fitness values and creates a new generation of spectral phases, which closes the feedback loop and restarts the first program part. The crucial part of any genetic algorithm is the protocol which decides which spectral phases will be kept for the next generation and which will be modified. This protocol will determine how fast the algorithm converges. The algorithm is considered converged once the optimum fitness parameter cannot be further increased within a range of values and loops defined by the operator. The protocol converging well on one objective may converge slowly on another. A converged result, i.e. here a spectral phase consisting of 640 entries for the 640 pixels, should be independent of the protocol chosen.

At the beginning of any optimization, neighboring parameters were binned together in five packs each containing 128 pixels. All parameters in one bin were given the same value. The binning size was decreased in the progress of the optimization between successive generations. This procedure is used to quickly approximate a rough structure in the parameter pattern and thus to speed up the convergence behavior. In general, the binning size reaches a value of 1, i.e. each pixel is addressed independently of all neighboring pixels, after 28 generations. After obtaining the fitness values from the first program part for each generation the fitness of all individuals were sorted accordingly. The best seven individuals (elites) were transferred to the next generation without further modification. Other individuals were modified or crossbred. Optimal fitness values were usually obtained after around 40 generations.

As we will describe in more detail in the result section, we observe the presence of fast and slow CH_3^+ ions in our ToF distributions. The GA is also used for maximizing the ion yield ratio of these fast versus slow CH_3^+ ions. In general distinct peak maxima are observed for fast and slow CH_3^+ ions, both in forward and backward direction. Yet, the peaks are intrinsically in general not fully resolved. For this reason integration of the ion ToF spectra is not appropriate. Instead we simply pick the peak maxima from the ToF distributions. While forward and backward scattered signals were analyzed separately for the kinetic energy (KE) analysis described below, in the case of maximizing the ratio of fast versus slow ions forward and backward ToF signals were added. Thus, the peak maxima are added for the low kinetic energy CH_3^+ ions (Y_{max}(lower KE) $=$ $Y_{max,\,forward}$(lower KE) $+$ $Y_{max,\,backward}$(lower KE)) and the high kinetic energy CH_3^+ (Y_{max}(higher KE) $=$ $Y_{max,\,forward}$(higher KE) $+$ $Y_{max,\,backward}$(higher KE)) separately. The ratio of the two quantities, either Y_{max}(lower KE)/Y_{max}(higher KE) or Y_{max}(higher KE)/Y_{max}(lower KE), then defines the fitness parameter for this particular optimization task. If Y_{max} for either the slow or the fast CH_3^+ was below a certain threshold the fitness for this individual was set zero.

As mentioned above all ions formed in the laser-matter interaction are analyzed and detected in a home-made linear time-of-flight mass spectrometer [25]. The classical ToF equations imply that a thermal kinetic energy distribution of ions will lead to a Gaussian ToF shape [26]. As a particular KE is connected to a corresponding set

of velocity vectors with ends on the surface of a sphere, a mono-energetic KER on the other hand will translate into a rectangular ToF shape [27, 28]. In the latter case, the center of this rectangular peak, observed at t_0, corresponds to ions with velocity vectors perpendicular to the ToF axis. The minimum and maximum ToF observed then correspond to ions with initial velocity vectors parallel to the ToF axis.

The width of the rectangle in the ToF domain, Δt, scales with the square root of the initial kinetic energy, $E_{kin,0}$, as given in (1.5), where m is the ion mass, q the charge, and G_1 the field strength in the ion source [$(U_1 - U_2)/d$ where U_1 and U_2 are the voltages of the first and the second electric lenses, respectively] [27].

$$\Delta t = \frac{\sqrt{2m}}{q \cdot G_1} \sqrt{E_{kin,0}} \qquad (1.5)$$

This $E_{kin,0}$ can e.g. originate from the thermal properties of the sample, but also from intra-molecular Coulomb repulsion in the dissociation of a dication.

Ultimately, any ion ToF distribution can be reconstructed from a weighted sum of rectangles, where the width of the rectangle reflects the relevant kinetic energy, the height reflects the weighing factor, which e.g. also accounts for the proper ToF—energy conversion. A thermal KE distribution will thus transform to a Gaussian ToF distribution.

If the kinetic energy is large enough, ions with an initial velocity vector perpendicular to the ToF axis do not reach the detector before they travel off the spectrometer axis so far that they do not hit the sensitive area of the MCP detector and consequently are discriminated in our spectrometer setup. As described by (1.6) ions are discriminated, if the perpendicular component of the velocity $v_\perp$ is larger than the detector radius divided by the time of flight for ions with zero initial velocity parallel to the detector axis t_0. For a given absolute initial velocity ions are seen by the detector if they are emitted into a cone with specific solid angle. Angular discrimination often leads to dips in the ion ToF distribution giving rise to *forward* and *backward scattered* ions (ions with velocity vectors initially pointing towards or away from the detector). Since t_0 depends on the acceleration fields applied in the ion source, angular discrimination is more pronounced for small draw out fields than for large fields.

$$v_\perp > \frac{r_{Detector}}{t_0} \qquad (1.6)$$

To deduce the energy distribution corresponding to a specific ToF distribution a genetic algorithm based on the same principles as mentioned above can be applied. Ideally, the ToF distributions are symmetric in forward and backward direction. Clearly this is not the case for the current setup (c.f. Fig. 1.11), where the effective angular discrimination is slightly different for forward and backward direction. We take account of this fact by analyzing the forward and the backward part of the ToF distributions separately and averaging the result afterwards.

The parameter set of each individual, which is to be optimized, is the probability for observing ions at a specific kinetic energy. Each kinetic energy is transformed into

a rectangle in the ToF domain according to the equations discussed above. Summing up these rectangles ultimately leads to a calculated ToF distribution. The size of the parameter set depends on the maximum kinetic energy of the ions considered and the energy increments chosen. The latter is typically $\Delta E = 100$ meV for H_3^+, and 30 meV for CH_3^+.

In the first part of the program the relevant region in the ToF spectrum is selected. The edge of this range defines the maximum kinetic energy to be considered in the KED. Each KE considered is transformed into a rectangle in the ToF domain. In doing so, the angular discrimination of ions discussed above must be considered. The ToF for which the ions do not contribute to the temporal distribution are calculated and given an ion yield of zero. For all ToF for which the ions reach the detector a weighting factor reflecting the amount of ions per ToF at a given energy is taken into account.

As the goal of the optimization is a good agreement between the simulated and measured ToF signals, the fitness value is defined as the inverted root mean square (rms) between experimental ion yields and the simulated ion yields of the parameter set. Since the calculated ToF axis in general has non-constant increments (we arbitrarily chose to start with constant increments in the energy domain), we finally have to interpolate the experimental ToF data in order to be able to calculate the rms discussed above.

The fitness value obtained by this procedure is handed over to the second program part. The feedback and the generation of new parameter sets for the next generation follow the concept of the genetic algorithm method discussed above. For obtaining energy distributions, usually one generation contains 50 individuals, from which 15 are transferred to the next generation as elites without modification. Convergence is generally achieved after several ten thousand generations.

1.3 Results

This section is organized as follows. We start by discussing aspects of controlling ion yields by means of linear chirping the laser fields. This subsection will review recent data from [21]. In a second subsection we then turn to the control of ion yields employing quadratic chirp. We also briefly discuss some other approaches for systematically shaping femtosecond laser fields. Finally, in order to complement these systematic chirp variations we present results of ion yield control and kinetic energy analysis employing a genetic algorithm in a fourth subsection.

1.3.1 Control by Linear Chirp

As outlined in the introduction previous work had established a complete reaction path for the formation of H_3^+ ions from ethane elucidating the role of hydrogen migration in dissociative ionization [13, 19]. In order to shed more light on the electron and nuclear dynamics involved we decided to perform additional studies
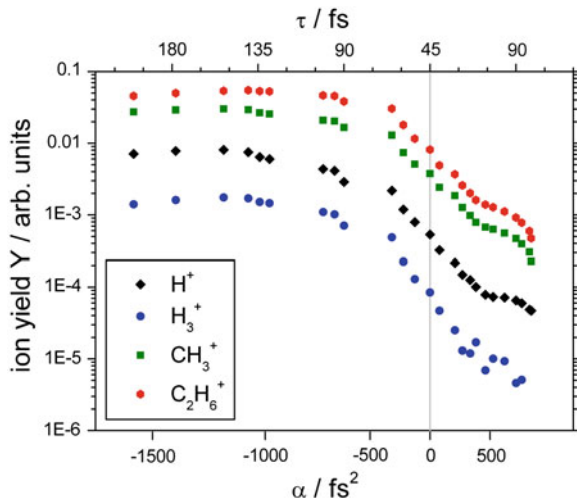
Fig. 1.3 Ion yields observed in the dissociative ionization of ethane as a function of the linear chirp parameter α (*lower axis*) and as a function of the pulse duration (*upper axis*). Note the logarithmic scale of the y axis. Data adapted from [21]

aiming at the control of branching ratios in the dissociative ionization of ethane. Here, it seems most appropriate to start by investigating the role of linear chirp in the dissociative ionization. Figure 1.3 shows the variation of ion yields with the linear chirp parameter α. Evidently the ion yields vary significantly with the sign as well as the value of the linear chirp parameter α [21]. All ion yields are maximized for values of α around $-1,200\,\text{fs}^2$.

This is a rather unique observation since most reports in the literature indicate that ion formation, in particular fragment ion formation, is intensity driven [29–31]. The latter, however, is not surprising for investigations conducted in the regime of $10^{14}\,\text{W/cm}^2$ and above. In contrast, our own studies showing pronounced chirp effects were performed at peak intensities on the order of $10^{12}\,\text{W/cm}^2$. Here, the dynamics is not in the strong field regime. On a qualitative basis we assume that a negative chirp is favorable for climbing an effectively anharmonic ladder of states compared to a positive chirp. For very high (positive and negative) chirp values the laser peak intensity decreases and leads to the observed decrease in ion yields. This is also the case for high negative chirps as this effect becomes more important. Clearly, further theoretical efforts are required in order to explain this chirp dependence. Ideally these calculations would combine high level theory for ionization as well as the dissociation of the ions.

Beyond this, also the ratio of e.g. H_3^+ to H^+ yields can be manipulated by choosing the appropriate chirp parameter [21]. The precondition for being able to control ion yields by means of chirping is again rather low laser intensity, on the order of $10^{12}\,\text{W/cm}^2$. At higher laser intensities, the dynamics involved become intensity driven implying maximum ion yields for the shortest pulse respectively the highest
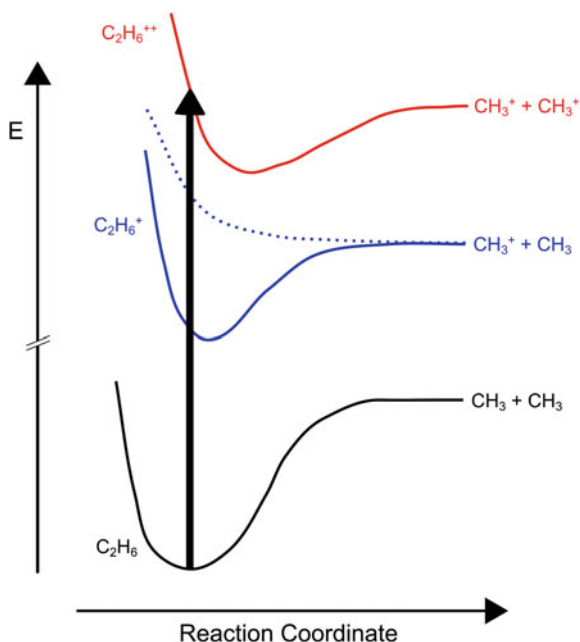
Fig. 1.4 Schematic illustration of the potential energy curves leading from neutral ethane (*lower curve*) to the formation of CH$_3^+$ ions either on the monocationic charge state (*middle curves*, note, there is certainly a bound potential energy curve but maybe also a repulsive one) or on the dicationic charge state (*upper curve*)

laser pulse peak intensities. Thus, the value of the chirp parameter α, for which the total ion yield is maximized, changes from about $-1,000\,\mathrm{fs}^2$ to zero when increasing the laser intensity from about $10^{12}\,\mathrm{W/cm}^2$ to a few times $10^{13}\,\mathrm{W/cm}^2$. Interestingly, the amount of fragmentation observed also increases with increasing negative chirp. For the lowest laser intensities accessible (15 µJ focused by a $\mathrm{f}=75\,\mathrm{mm}$ lens) the ratio of yields $\mathrm{Y(H_3^+):Y(H^+)}$ is maximized for a chirp of $\alpha = -700\,\mathrm{fs}^2$. Since the two ions predominantly originate from the same charge state as illustrated in Fig. 1.1, i.e. the dication state, we discussed this as an example of an *intra-charge-state* control, implying aspects of the control and localization of electron density.

On the other hand, the formation of CH$_3^+$ ions may proceed either on the same dicationic state or on the monocationic state as illustrated in Fig. 1.4. The two different charge states transform to significantly different average KER into the fragments, one being on the order of 2.7 eV, the other on the order of 0.7 eV [21]. While the KER of 2.7 eV is in line with the Coulomb explosion of a doubly charged ethane ion, the KER of 0.7 eV most likely involves impulsive fragmentation from a repulsive state of the mono charged cation. The dissociation on the ground state of the ethane monocation would lead to a thermal KER not compatible with the findings. Ultimately we were able to demonstrate that linear chirp allows to control the yields of slow CH$_3^+$ ions versus fast CH$_3^+$ ions. We consider this to be an example of *inter-charge-state* control.
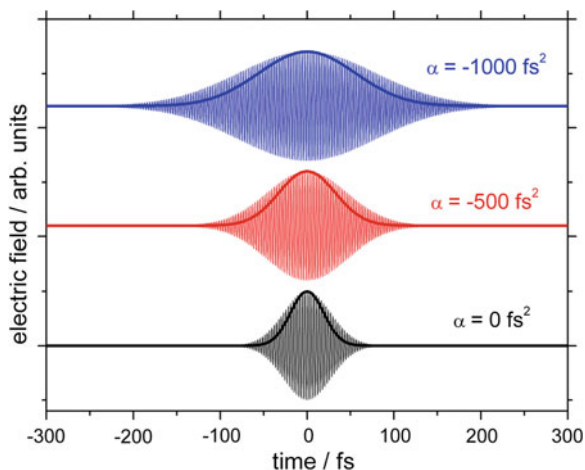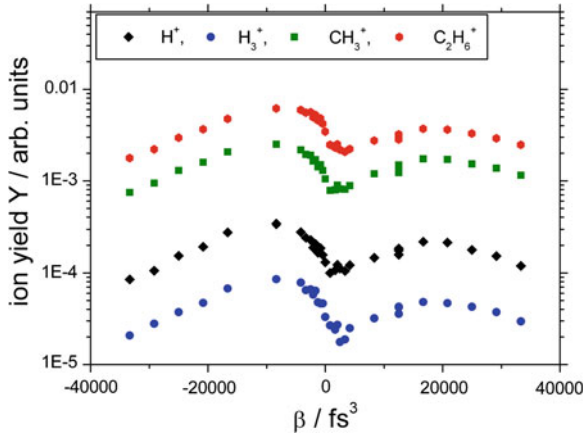
Fig. 1.5 Illustration of laser fields for an unchirped laser pulse (*lower trace*), $\alpha = -500\,\text{fs}^2$ (*middle trace*) and $\alpha = -1,000\,\text{fs}^2$ (*upper trace*). Center wavelength is 810 nm and the FWHM of the shortest pulse is 45 fs. Also shown is in each case the temporal intensity as a thick *solid line*. All traces normalized to the same arbitrary value, i.e. 1

To conclude this subsection on the role of linear chirp it appears helpful to visualize typical laser fields employed in the studies presented above. To this end, Fig. 1.5 shows these laser fields for the 45 fs pulse, for $\alpha = -500\,\text{fs}^2$ and for $\alpha = -1,000\,\text{fs}^2$. Note, the traces have all been normalized to the same arbitrary maximum amplitude of 1, in order to highlight the variation in pulse duration. In addition Fig. 1.5 also includes the three temporal intensity profiles, again normalized to 1. With increasing chirp parameter the pulse duration increases quadratically as can be seen from (1.3).

1.3.2 Control by Quadratic Chirp

As we have demonstrated in previous work [21] and also in the previous section, the dynamics of ethane ionization/dissociation can be strongly influenced by the linear chirp parameter α. Are higher order contributions to the spectral phase of similar importance? In order to answer this question we have performed a systematic variation of quadratic chirp (TOD) β for various values of α.

Figure 1.6 presents yields for the parent ion $C_2H_6^+$, as well as fragment ions CH_3^+, H_3^+ and H^+. Evidently, all ion yields shown exhibit a maximum at values $\beta = -8,333\,\text{fs}^3$. A minimum is observed for all ions analyzed at values $\beta = +2,500\,\text{fs}^3$. For positive values of β the ion yields exhibit another, local maximum at $\beta = +16,666\,\text{fs}^3$. Overall, the yield curves are highly asymmetric with respect to $\beta = 0\,\text{fs}^3$. Large β parameters correspond to pulse sequences effectively spread out over longer times, thus reducing the actual light intensity. In Fig. 1.7 we
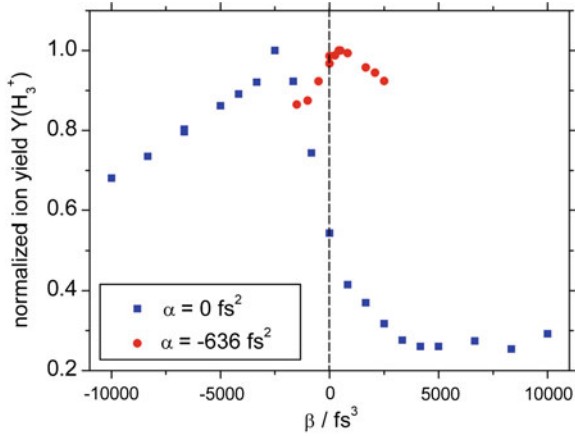
Fig. 1.6 Ion yields of some species observed in the ionization/dissociation of ethane as a function of the quadratic chirp parameter β. Note the logarithmic y axis. The laser pulse energy was 15 µJ/pulse, $\alpha = 0\,\mathrm{fs}^2$
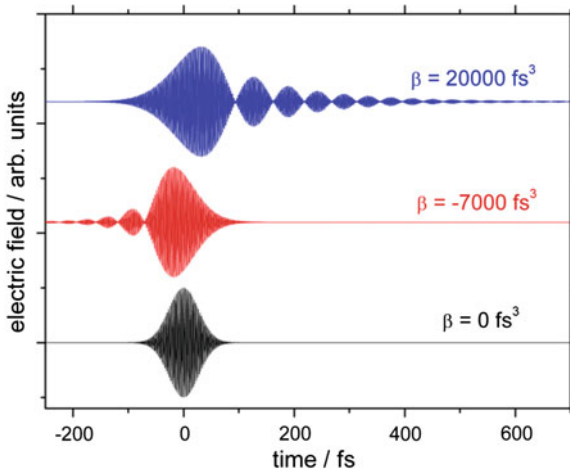
Fig. 1.7 Illustration of laser fields for an unchirped laser pulse (*lower trace*), $\beta = -7{,}000\,\mathrm{fs}^3$ (*middle trace*) and $\beta = +20{,}000\,\mathrm{fs}^3$ (*upper trace*). Center wavelength is 810 nm, the FWHM of the unchirped pulse is 45 fs

again illustrate laser fields for typical values of $\beta = 0\,\mathrm{fs}^3$, $\beta = -7{,}000\,\mathrm{fs}^3$, and $\beta = +20{,}000\,\mathrm{fs}^3$. E.g. for $\beta = +20{,}000\,\mathrm{fs}^3$ the effective laser field is spread out over several 100 fs. Note that a positive sign of β implies a distortion towards positive time (i.e. trailing part of the light-matter interaction), a negative sign of β implies a distortion towards negative time (i.e. leading part of the light-matter interaction). The decrease of ion yields for very large positive or negative β may be explained by

Fig. 1.8 H_3^+ ion yields observed in the ionization/dissociation of ethane as a function of the quadratic chirp parameter β for $\alpha = 0\,\text{fs}^2$ and for a negative linearly chirped laser pulse. Pulse energy: $50\,\mu\text{J/pulse}$

the concomitant decrease in light intensity. The case $\beta = 0\,\text{fs}^3$ is not a particularly favorable spectral phase in terms of ion yields.

It appeared appropriate to start the discussion of TOD effects by setting all other contributions to the spectral phase equal to zero, i.e. looking at pure TOD effects. The obvious next question is: are TOD effects still important if we set the linear chirp parameter to a value where one of our objectives is maximized, e.g. the H_3^+ ion yield or the ratio of yields $Y(H_3^+) : Y(H^+)$. For this purpose additional experiments have been performed at slightly increased pulse energy (50 µJ/pulse). Figure 1.8 shows the H_3^+ ion yield as a function of β for a linear chirp parameter $\alpha = -636\,\text{fs}^2$, a value close to the one for which the H_3^+ ion yield was maximized for a pure linear chirp [21]. We note that for $\alpha = -636\,\text{fs}^2$ the maximum of the H_3^+ ion yield is observed very close to $\beta = 0\,\text{fs}^3$. Thus one may conclude that the linear chirp is more important than the quadratic chirp. For comparison the graph also shows the β variation for $\alpha = 0\,\text{fs}^2$. It appears that the entire data set has been shifted to more positive β values compared to Fig. 1.6.

The laser fields associated with the maxima observed in Fig. 1.8 are displayed in Fig 1.9. Evidently, the laser field for chirp parameters $\alpha = 0\,\text{fs}^2$, $\beta = -2,500\,\text{fs}^3$ is very different from that for $\alpha = -636\,\text{fs}^2$, $\beta = 500\,\text{fs}^3$. On the other hand the latter is hardly distinguishable from the laser field for parameters $\alpha = -636\,\text{fs}^2$, $\beta = 0\,\text{fs}^3$. This lends further support to the conclusion that the linear chirp parameter is more important than the quadratic chirp parameter in the dissociative fs-laser ionization of ethane.

There are rather few reports on systematic investigations of quadratic chirp in the literature, perhaps because of its subordinate role. As one example we note the work by Wollenhaupt et al. demonstrating the importance of quadratic chirp in photoionization dynamics governing the material processing relevant for microprocessing [32].
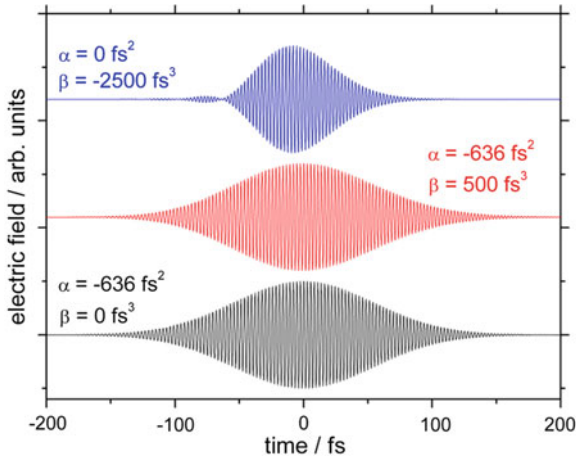
Fig. 1.9 Illustration of laser fields for $\alpha = 0\,\text{fs}^2, \beta = -2,500\,\text{fs}^3$ (*upper trace*), for $\alpha = -636\,\text{fs}^2$, $\beta = 500\,\text{fs}^3$ (*middle trace*) and for $\alpha = -636\,\text{fs}^2, \beta = 0\,\text{fs}^3$ (*lower trace*). Center wavelength is 810 nm, the FWHM of the shortest pulse is 45 fs

1.3.3 Control by Other Means of Systematic Pulse Shaping

We briefly recall some other approaches for systematic pulse shaping known and applied in the literature. First, we mention binary pulse shaping where successive phase jumps of π are written to a SLM [33, 34]. This approach has been successfully applied by Dela Cruz for distinguishing p-xylene and o-xylene structural isomers [35]. We note, that this distinction is also possible by means of systematic linear chirp [36].

We also mention femtosecond interferometry as a means for systematically shaping an effective laser field. Here, the original laser pulse is split into two identical replicas in a Michelson interferometer. Combining the two partial laser fields as a function of the length of the two arms leads to interference phenomena. Changing the delay time between the two arms of the interferometer then leads to a variation of the integrated laser intensity which in turn leads to a variation of the corresponding ion yields. If aligned with the necessary care the laser fields obtained by this interferometry allow to investigate in particular highly non-linear dynamical process, e.g. the formation of H_3^+ from ethane as shown in Fig. 1.10. Translating the movable mirror in steps of 10 nm then corresponds to a change in the delay time of about 60 as giving access to extremely high relative time resolution. Ultimately we expect that this approach might provide excess to a better understanding of the coupling of electron and nuclear dynamics [37, 38].
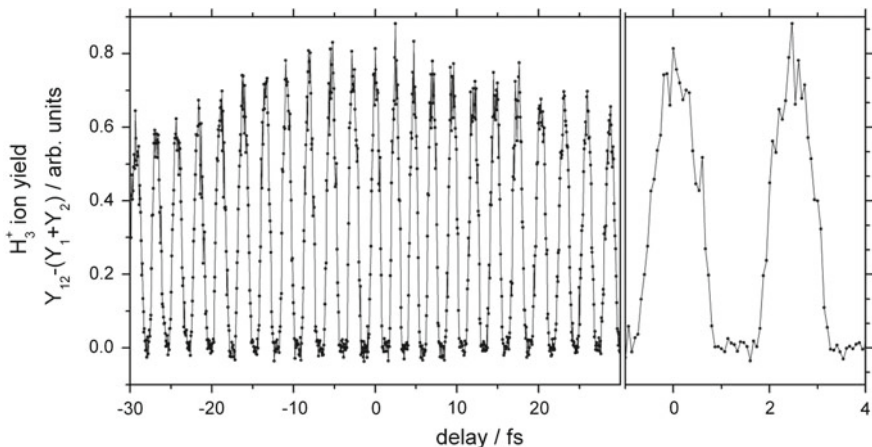
Fig. 1.10 Interferogramm for the formation of H_3^+ ions recorded at a chosen central wavelength of 800 nm and 15 μJ pulse energy in each arm of the interferometer, starting from unchirped pulses. Y_{12} is the interferometric signal; Y_1 and Y_2 are the signals for arm 1 and 2 at infinite temporal separation of the partial waves. Note, the time steps are 60 as. The stability of the interferometer is on the order of 120 as

1.3.4 Control by Genetic Algorithm

In previous sections we have investigated the role of linear and quadratic chirp on the yields of ions formed in the dissociative ionization of ethane. We now investigate the possible interplay of chirp contributions from different orders. In other words we search for the optimum spectral phase with respect to a given objective, e.g. maximizing a specific ion yield. This is a classical question for optimal control studies [39–41]. One of the central goals of the current investigation is the understanding and control of H_3^+ formation. Consequently, we first attempt to find the optimum laser field which maximizes the H_3^+ ion yield in the dissociative ionization of ethane. This goal is approached by using a 4f-shaper with a spatial light modulator for which the spectral phase is imprinted on 640 pixels. Thus, the phase shift for each pixel, i.e. each wavelength, can be varied independently and optimized by the genetic algorithm mentioned above (see experimental section). Figure 1.11 shows the ToF-MS of the H_3^+ ion region for the optimized laser field (upper trace) and for comparison the ToF-MS for an unchirped laser field at the same pulse energy (lower trace). In the case of the optimized laser field the total yield of the H_3^+ ion is about a factor of 8 higher than in the case of 45 fs pulses. This variation is considered a rather large value. More typical values reported in the literature are factors of 2 or 3 [39, 42, 43].

We now attempt to illustrate the characteristics of the underlying control scheme. To this end we show the FROG trace of the optimized laser field in Fig. 1.12a. We first note that the overall temporal width of the pulse is on the order of 130 fs, which matches with the findings of the systematic variation of the linear chirp at the
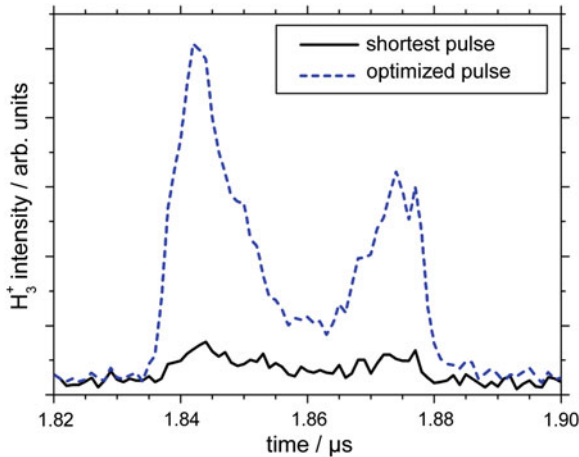
Fig. 1.11 H_3^+ TOF signal for the unchirped pulse (*black*), and for the genetic algorithm optimized pulse (*blue*). The pulse energy is 17 µJ/pulse

corresponding pulse energy [21]. Also, the spectral phase retrieved by the FROG algorithm suggests a predominance of a linear chirp. The SHG-FROG used in our experiment is capable of identifying a linear chirp, however it is not able to distinguish between a negative and positive chirp. Nevertheless we are able to characterize the pulses to the level desired by writing that spectral phase to the SLM which transforms the pulse found by optimization back into the shortest achievable laser pulse. In the case of the laser pulse presented in Fig. 1.12a writing a linear chirp with $\alpha = +900\,\text{fs}^2$ and a quadratic chirp with $\beta = -3{,}333\,\text{fs}^3$ to the SLM generates a close to 45 fs pulse depicted in Fig. 1.12c. Thus we conclude that the originally optimized laser pulse was dominated by linear and quadratic chirp components of $\alpha = -900\,\text{fs}^2$ and $\beta = +3{,}333\,\text{fs}^3$ respectively.

It is interesting to analyze the kinetic energy distribution of the H_3^+ ions formed with the optimized laser field. The procedure for this analysis was described in the experimental section. Figure 1.13 presents the kinetic energy distribution of the H_3^+ ions formed with the optimized laser field discussed above. Evidently the KED is spread out over more than 2 eV with the maximum probability occurring in the region of 3 eV. The overall KED shown here is very similar to the one reported by Kanya et al. [19], however the maximum probability occurred at slightly larger values there. Note that the KE's we discuss in this work refer to a specific fragment, here the H_3^+, while the total KE released into all fragments was reported in [19]. For the $C_2H_6^{++} \rightarrow H_3^+ + C_2H_3^+$ channel the ratio between the total KER and the $KE(H_3^+)$ is 10 : 9. This small difference of 10 % does not fully account for the difference between the current KED and the one reported in [19]. At this point we cannot answer the question whether the KED depends on the fs-pulse shape. Further studies are required to resolve this issue.
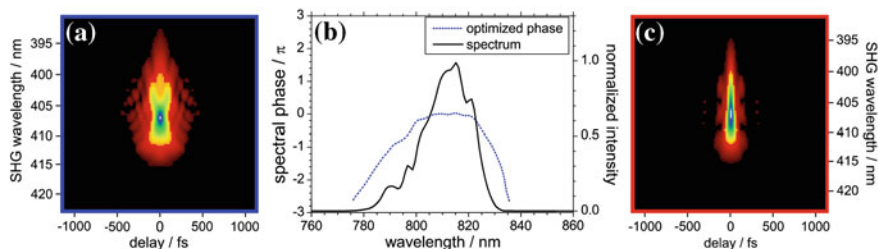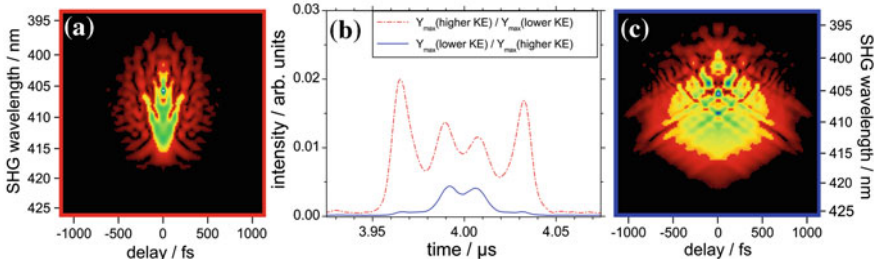
Fig. 1.12 a FROG of laser pulse optimized for H_3^+ (17 µJ), FWHM = 128 fs; **b** Spectrum and spectral phase retrieved from FROG; **c** FROG of the recompressed laser pulse obtained by adding a linear chirp with $\alpha = +900\,fs^2$ and a quadratic chirp with $\beta = -3,333\,fs^3$ to the pulse shown in (**a**). Hence, the main chirp components of the optimized pulse (**a**) are $\alpha = -900\,fs^2$, $\beta = +3,333\,fs^3$. The *vertical axis* of the FROG pictures is the SHG-wavelength in nm, the *horizontal axis* is the delay in fs
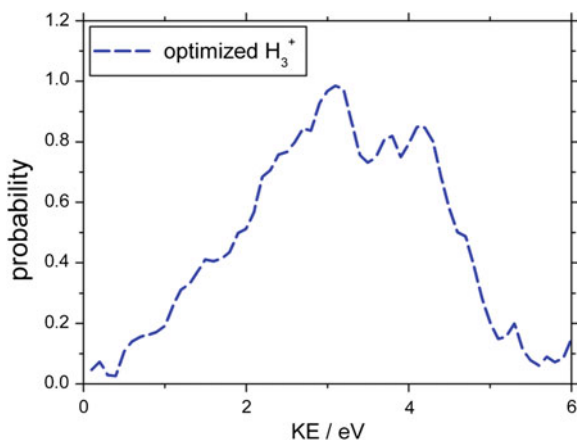
Fig. 1.13 Kinetic energy distribution of the H_3^+ ions formed via the optimized laser field

We have also performed GA studies for optimizing the H_3^+ ion yield at higher pulse energies. For a pulse energy of 80 µJ (not shown here) the optimal laser pulse found by the genetic algorithm has a pulse duration of about 60 fs. This is a little (but discernibly) longer than the duration of the shortest pulse achieved. Consequently a small linear chirp of $\alpha = 350\,fs^2$ has to be added to this pulse in order to recompress it to the shortest one. Therefore, the main chirp component of the optimized pulse is concluded to be $\alpha = -350\,fs^2$. This result matches the findings reported in [21]. With increasing pulse energy the dynamics become intensity driven and linear and quadratic chirp is not favoring high ion yields.

The comparison of results from systematically adding linear or quadratic chirp to a laser field with results from GA optimization demonstrates that systematic variation of chirp parameters is an efficient tool for maximizing ion yields for H_3^+ ions as well as for H^+ ions (the latter not shown here). The introduction of more complicated

**Fig. 1.14** **a** FROG of laser pulse optimized for Y_{max}(higher KE)/Y_{max}(lower KE) (82 µJ), FWHM = 116 fs; **b** CH_3^+ ion yields optimized for Y_{max}(higher KE)/Y_{max}(lower KE) (*red*) and Y_{max}(lower KE)/Y_{max}(higher KE) (*blue*); **c** FROG of laser pulse optimized for Y_{max}(lower KE)/Y_{max}(higher KE) (80 µJ) FWHM >400 fs. All information referring to the CH_3^+ ion. The *vertical axis* of the FROG pictures is the SHG-wavelength in nm, the *horizontal axis* is the delay in fs

spectral phases with a genetic algorithm does not cause significantly better results than already obtained with systematic chirp.

In Sect. 1.3.1 we have mentioned the ability to control the ratio of fast CH_3^+ ions (originating from the dicationic state) to slow CH_3^+ ions originating from the monocationic state of ethane. In the following we search for the optimum laser field for maximizing the ratio of ion yields of slow to fast CH_3^+ ions, (Y_{max}(lower KE)/Y_{max}(higher KE), and vice versa. Since the peaks for fast and slow components of CH_3^+ are not always well separated, integration of ion yields is not the method of choice. Instead we analyze the maximum signal amplitudes at the respective peak positions.

Figure 1.14a, c show FROG traces obtained for optimizing the ion yield ratios Y_{max}(higher KE)/Y_{max}(lower KE) and Y_{max}(lower KE)/Y_{max}(higher KE) respectively. The corresponding ion yields themselves are shown in Fig. 1.14b. Overall, the ion yield ratio Y_{max}(higher KE)/Y_{max}(lower KE) can be changed from about 1 : 5 to 2 : 1.

Further analysis of the FROG traces shows that the laser pulse maximizing the ratio Y_{max}(higher KE)/Y_{max}(lower KE) (Fig. 1.14a) can be recompressed from about 116 fs to 52 fs by mainly adding a negative linear chirp of $\alpha = -550 \, fs^2$. Other more complex phase components are present but of minor importance. For the laser pulse depicted in Fig. 1.14c, i.e. the one optimizing the ratio Y_{max}(lower KE)/Y_{max}(higher KE) we do not find a simple spectral phase characteristic. We note that the overall temporal pulse width is in this case larger than 400 fs. Since both optimizations were conducted at a pulse energy of about 80 µJ/pulse the smaller temporal width of the pulse in Fig. 1.14a implies a considerably higher intensity compared to the pulse in Fig. 1.14c. The higher laser intensity ultimately favors the fast component of the CH_3^+ ions, which originate from doubly ionized ethane ions. This adds to a self-consistent picture. The laser field in Fig. 1.14c is very complex. We note that in the maximization of the ratio Y_{max}(lower KE)/Y_{max}(higher KE) effectively
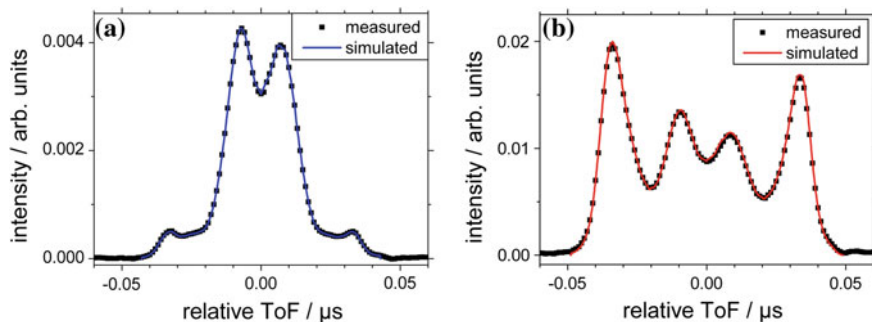
Fig. 1.15 Optimal control of CH_3^+ ion yields. **a** *Left graph* ToF-MS for a laser field maximizing the ratio Y_{max}(lower KE)/Y_{max}(higher KE). **b** *Right graph* ToF-MS for a laser field maximizing the ratio Y_{max}(higher KE)/Y_{max}(lower KE)
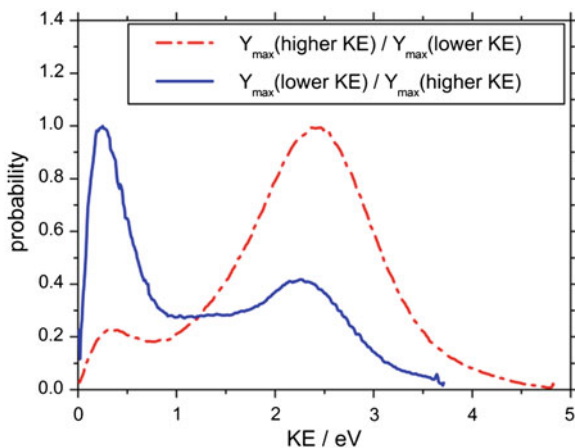
Fig. 1.16 Kinetic energy distributions for optimized laser fields: *solid line* maximization of the ratio Y_{max}(lower KE)/Y_{max}(higher KE). *dotted line* maximization of the ratio Y_{max}(higher KE)/Y_{max}(lower KE)

the total yield of both fast and slow ions is decreased, but the fast component is even stronger suppressed than the slow component.

The ToF spectra (recorded at a pressure of 3.9×10^{-6} mbar) shown in Fig. 1.14b evidently involve very different KE distributions of the CH_3^+ ions. In order to quantify this observation we have again performed a KE analysis. Figure 1.15 shows the relevant experimental ToF spectra together with the best simulations, which is based on the KE distributions displayed in Fig. 1.16.

The two KED's shown in Fig. 1.16 both exhibit probability maxima at about 0.4 eV and at 2.5 eV. However the relative peak probability differs significantly. For optimization of the slow versus fast component the ratio of peak values is 1:0.4, while for optimization of the fast versus slow component it is 0.2:1. While previous

analysis only extracted average KER from the ToF spectra we have arrived at a more detailed picture here by presenting the entire KED's.

1.4 Summary and Conclusions

We have presented a systematic investigation of the influence of pulse shaping on the formation of fragment ions in the dissociative ionization of ethane employing intense ultra-short laser pulses. We have demonstrated that concepts aiming at understanding and those aiming at controlling go hand in hand. E.g., previous work directed at understanding the dynamics had provided evidence for hydrogen scrambling within the dicationic state of ethane. Additional experiments with the goal of controlling the yields of fragment ions as well as their properties (here the kinetic energy) have shed additional light on the mechanisms involved. In particular we see clear evidence of intra-charge-state control as well as inter-charge-state control. This opens access to improved understanding of the competition between single ionization and double ionization. Ultimately it is hoped that experimental work as outlined here stimulates further theoretical investigation in order to better understand the electron and nuclear dynamics involved in the dissociative ionization of small hydrocarbon molecules.

References

1. A. Giusti-Suzor, F.H. Mies, L.F. DiMauro, E. Charron, B. Yang, J. Phys. B: At. Mol. Opt. Phys. **28**, 309 (1995)
2. B. Sheehy, L.F. DiMauro, Annu. Rev. Phys. Chem. **47**, 463 (1996)
3. S.A. Buzza, E.M. Snyder, D.A. Card, D.E. Folmer, A.W. Castleman, J. Chem. Phys. **105**, 7425 (1996)
4. M.J. Dewitt, D.W. Peters, R.J. Levis, Chem. Phys. **218**, 211 (1997)
5. J.H. Posthumus, Rep. Prog. Phys. **67**, 623 (2004)
6. I.V. Hertel, W. Radloff, Rep. Prog. Phys. **69**, 1897 (2006)
7. A. Vredenborg, C.S. Lehmann, D. Irimia, W.G. Roeterdink, M.H.M. Janssen, Chemphyschem **12**, 1459 (2011)
8. Q.L. Liu, J.K. Wang, A.H. Zewail, Nature **364**, 427 (1993)
9. H. Arnolds, M. Bonn, Surf. Sci. Rep. **65**, 45 (2010)
10. R. Itakura, P. Liu, Y. Furukawa, T. Okino, K. Yamanouchi, and H. Nakano, J. Chem. Phys. **127**, 104306 (2007)
11. C.Y. Wu, Q.Q. Liang, M. Liu, Y.K. Deng, Q.H. Gong, Phys. Rev. A **75**, 043408 (2007)
12. K. Hoshina, Y. Furukawa, T. Okino, K. Yamanouchi, J Chem Phys **129**, 104302 (2008)
13. P.M. Kraus, M.C. Schwarzer, N. Schirmel, G. Urbasch, G. Frenking, K.-M. Weitzel, J. Chem. Phys. **134**, 114302 (2011)
14. H. Conroy, J. Chem. Phys. **40**, 603 (1964)
15. W. Koch, G. Frenking, J. Gauss, D. Cremer, J. Am. Chem. Soc. **108**, 5808 (1986)
16. M.D. Burrows, S.R. Ryan, W.E. Lamb, L.C. Mcintyre, J. Chem. Phys. **71**, 4931 (1979)

17. T. Okino, Y. Furukawa, P. Liu, T. Ichikawa, R. Itakura, K. Hoshina, K. Yamanouchi, H. Nakano, Chem. Phys. Lett. **419**, 223 (2006)
18. T. Okino, Y. Furukawa, P. Liu, T. Ichikawa, R. Itakura, K. Hoshina, K. Yamanouchi, H. Nakano, Chem. Phys. Lett. **423**, 220 (2006)
19. R. Kanya, T. Kudou, N. Schirmel, S. Miura, K.-M. Weitzel, K. Hoshina, K. Yamanouchi, J. Chem. Phys. **136**, 204309 (2012)
20. J.H.D. Eland, Rapid Commun. Mass Spectrom. **10**, 1560 (1996)
21. N. Schirmel, N. Reusch, P. Horsch, K.-M. Weitzel, Faraday Discuss. **163**, 461–474 (2013)
22. P. Balling, D.J. Maas, L.D. Noordam, Phys. Rev. A **50**, 4276 (1994)
23. R. Trebino, in *Frequency-Resolved Optical Gating: The Measurement of Ultrashort Laser Pulses* (Kluwer Academic Publishers, Norwell, 2000)
24. D.E. Goldberg, in *Genetic Algorithms in Search, Optimization, and Machine Learning* (Addison-Wesley, Reading, UK, 1993)
25. W.C. Wiley, I.H. McLaren, Rev. Sci. Instrum. **26**, 1150 (1955)
26. R. Stockbauer, Int. J. Mass Spectrom. Ion Phys. **25**, 89 (1977)
27. J.L. Franklin, P.M. Hierl, D.A. Whan, J. Chem. Phys. **47**, 3148–3153 (1967)
28. K.-M. Weitzel, F. Güthe, J. Mähnert, R. Locht, H. Baumgärtel, Chem. Phys. **201**, 287 (1995)
29. R. Itakura, K. Yamanouchi, T. Tanabe, T. Okamoto, F. Kannari, J. Chem. Phys. **119**, 4179 (2003)
30. D. Mathur, F.A. Rajgara, J. Chem. Phys. **120**, 5616 (2004)
31. V.V. Lozovoy, X. Zhu, T.C. Gunaratne, D.A. Harris, J.C. Shane, M. Dantus, J. Phys. Chem. A **112**, 3789 (2008)
32. M. Wollenhaupt, L. Englert, A. Horn, T. Baumert, J. Laser Micro Nanoeng. **4**, 144 (2009)
33. M. Comstock, V.V. Lozovoy, I. Pastirk, M. Dantus, Opt. Express **12**, 1061 (2004)
34. V.V. Lozovoy, T.C. Gunaratne, J.C. Shane, M. Dantus, Chemphyschem **7**, 2471 (2006)
35. J.M. Dela Cruz, V.V. Lozovoy, M. Dantus, J. Phys. Chem. A **109**, 8447 (2005)
36. G. Urbasch, H.G. Breunig, K.M. Weitzel, Chemphyschem **8**, 2185 (2007)
37. H.G. Breunig, G. Urbasch, K.M. Weitzel, J. Chem. Phys. **128**, 121101 (2008)
38. M.V. Korolkov, K.M. Weitzel, Chem. Phys. Lett. **487**, 209 (2010)
39. A. Assion, T. Baumert, M. Bergt, T. Brixner, B. Kiefer, V. Seyfried, M. Strehle, G. Gerber, Science **282**, 919 (1998)
40. R. Kosloff, S.A. Rice, P. Gaspard, S. Tersigni, D.J. Tannor, Chem. Phys. **139**, 201 (1989)
41. S.A. Rice, M.S. Zhao, in *Optical Control of Molecular Dynamics* (Wiley, New York, 2000)
42. M. Bergt, T. Brixner, B. Kiefer, M. Strehle, G. Gerber, J. Phys. Chem. A **103**, 10381 (1999)
43. H.G. Breunig, A. Lauer, K.M. Weitzel, J. Phys. Chem. A **110**, 6395 (2006)

Progress in Ultrafast Intense Laser Science XI
Yamanouchi, K.; Nam, C.H.; Martin, P. (Eds.)
2015, XV, 238 p. 127 illus., 56 illus. in color., Hardcover